Acta Pharmaceutica Sinica B 2022;12(11):4235–4248

Chinese Pharmaceutical Association
Institute of Materia Medica, Chinese Academy of Medical Sciences

Acta Pharmaceutica Sinica B

www.elsevier.com/locate/apsb
www.sciencedirect.com

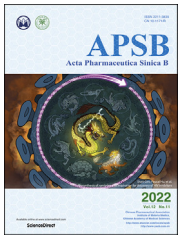

ORIGINAL ARTICLE

Broad-spectrum and powerful neutralization of bacterial toxins by erythroliposomes with the help of macrophage uptake and degradation

Chunying Liu[a], Shuangrong Ruan[b], Ying He[a], Xuejing Li[a], Yuefei Zhu[a,c], Honglan Wang[d], Hanwei Huang[a], Zhiqing Pang[a,*]

[a]*School of Pharmacy, Fudan University, Key Laboratory of Smart Drug Delivery, Ministry of Education, Shanghai 201203, China*
[b]*The Institute for Biomedical Engineering & Nano Science, Tongji University School of Medicine, Shanghai 200092, China*
[c]*Department of Biomedical Engineering, Columbia University, New York, NY 10027, USA*
[d]*Institute of Hematology, Union Hospital, Tongji Medical College, Huazhong University of Science & Technology, Wuhan 430022, China*

Received 30 December 2021; received in revised form 14 January 2022; accepted 8 February 2022

KEY WORDS

Erythroliposome;
Broad-spectrum detoxification;
Hybrid nanovesicle;
Pore-forming toxins;
Macrophage uptake;
Red blood cell membrane;
Artificial lipid membrane

Abstract Anti-virulence strategy has been considered as one of the most promising approaches to combat drug-resistant bacterial infections. Pore-forming toxins (PFTs) are the largest class of bacterial toxins, inflicting their virulence effect through creating pores on the cell membrane. However, current solutions for eliminating PFTs are mostly designed based on their molecular structure, requiring customized design for different interactions. In the present study, we employed erythroliposome (denoted as RM-PL), a biomimetic platform constructed by artificial lipid membranes and natural erythrocyte membranes, to neutralize different hemolytic PFTs regardless of their molecular structure. When tested with model PFTs, including α-hemolysin, listeriolysin O, and streptolysin O, RM-PL could completely inhibit toxin-induced hemolysis in a concentration-dependent manner. *In vivo* studies further confirmed that RM-PL could efficiently neutralize various toxins and save animals' lives without causing damage to organs or tissues. In addition, we explored the underlying mechanisms of this efficient detoxification ability and found that it was mainly macrophages in the spleen and the liver that took up RM-PL-absorbed toxins through a variety of endocytosis pathways and digested them in lysosomes. In summary, the biomimetic RM-PL presented a promising system for broad-spectrum and powerful toxin neutralization with a mechanism of lysosome-mediated toxin degradation.

*Corresponding author. Tel./fax: +86 21 51980069. .
E-mail address: zqpang@fudan.edu.cn (Zhiqing Pang).

Peer review under responsibility of Chinese Pharmaceutical Association and Institute of Materia Medica, Chinese Academy of Medical Sciences

https://doi.org/10.1016/j.apsb.2022.03.015

2211-3835 © 2022 Chinese Pharmaceutical Association and Institute of Materia Medica, Chinese Academy of Medical Sciences. Production and hosting by Elsevier B.V. This is an open access article under the CC BY-NC-ND license (http://creativecommons.org/licenses/by-nc-nd/4.0/).

© 2022 Chinese Pharmaceutical Association and Institute of Materia Medica, Chinese Academy of Medical Sciences. Production and hosting by Elsevier B.V. This is an open access article under the CC BY-NC-ND license (http://creativecommons.org/licenses/by-nc-nd/4.0/).

1. Introduction

Bacterial infections have been conventionally controlled by antibiotics since the discovery of penicillin in 1940s[1], and this approach saved countless lives and enabled the development of modern medicine[2]. However, the extensive and uncritical use of antibiotics in humans, animals, agriculture and the food chain without careful consideration of the societal consequences[3], following the strong selection pressure imposed on bacteria, increased the rate of antibacterial resistance, which is acknowledged as one of the world's most urgent health problems. It has been estimated that antibiotic resistance kills 700,000 people each year worldwide, and some experts believe that the number could rise to 10 million by 2050 if efforts are not made to address resistance or develop new antibiotics[4]. However, the clinical antibacterial pipeline, dominated by derivatives of established antibiotic classes, is not very encouraging[2,3,5,6]. There is a growing body of literature that recognizes the importance of developing new therapies without cross-resistance to existing antibiotics to fight bacterial infections[1,7].

One promising approach that has gained attention recently involves choosing bacterial virulence mechanisms as targets for therapy[8,9]. Pore-forming toxins (PFTs) represent the largest class of bacterial toxins, comprising about 25%−35% of all known bacterial virulence factors[10−12]. They are secreted as water-soluble monomers, assemble into oligomeric pores on the plasma membrane of target cells, and therefore can initiate an assortment of downstream responses, facilitating the growth and dissemination of causative bacteria[10]. It has been well documented that for many of the most important bacterial pathogens, severe infection is fueled by the cell damaging and pro-inflammatory effects of PFTs[13]. This is evident in the case of *Staphylococcus aureus* lacking α-toxin, which shows attenuation in animal infection models[13]. Most importantly, a fair amount of existing and emergent multidrug resistant bacteria, so-called "superbugs" such as methicillin-resistant *S. aureus*, secrete a variety of highly potent PFTs with no currently available antitoxins on the market[14]. This knowledge motivated the development of multi-model strategies to neutralize or counteract their toxicity as an innovative pharmacological approach to combat the infectious diseases. Given that the anti-virulence strategies do not focus on directly killing the pathogen, they exert less selective pressure on bacteria, which are less susceptible to resistance development[15,16], while preserving the normal host microbiome.

Conventional solutions for eliminating PFTs are mostly created based on the molecular structure of PFTs, requiring customized design for different interactions[17,18]. In view of the fact that one bacteria species can secrete several PFTs, and the enormous diversity of bacterial virulence factors, such structure-based strategies have been challenged by an overwhelming number of distinctive molecular structures and epitopic targets[19]. Therefore, it is necessary to develop a novel function-based, rather than structure-based, toxin removal approach to achieve broad-spectrum toxin clearance[20]. Owing the pore-forming principles shared by most PFTs and its close connections with the cellular membrane, a biomimetic nanoparticle design has recently emerged by wrapping polymeric core with red blood cell (RBC) membranes (denoted as nanosponges), which has been shown to display great broad-spectrum toxin neutralization capacity both *in vitro* and *in vivo*[21−23]. Meanwhile, artificial liposomes containing sphingomyelin and a high cholesterol content, which provide the basic lipid bilayer structure to preoccupy and neutralize toxin actions, were also fabricated to sequester various bacterial PFTs[24]. However, when the bacterial infection progressed, the detoxification capacity of nanosponges or artificial liposomes as biodetoxification nanoagents was challenged. In addition, the complicated cell membrane coating process and the scale-up problem made the production of nanosponges on large scale difficult. Moreover, the coating process might destroy cell membrane proteins and therefore decrease the detoxification capacity. For this reason, biodetoxification nanoagents with high detoxification capacities and simple production processes are urgently needed for antivirulence therapy. According to the pore-forming process of PFTs, the recognition and binding of PFTs rely only on a specific small region on the natural cell membrane, indicating that a small fraction of the cell membrane might effectively detoxify PFTs. Thus, exploiting artificial lipid membranes to replace most of the natural cell membrane holds great promise in maintaining or even enhancing the detoxification capacity of the cell membrane and ultimately economizing this property. Moreover, compared with natural cell membranes, artificial lipid membranes are more easily modified and more feasibly scaled up. This knowledge has inspired us to design a hybrid nanovesicle by fusing lipid membranes and RBC membranes (RM-PL, denoted as erythroliposome) for amplified biodetoxification, which takes advantages of both the basic membrane structure provided by artificial lipids and the PFT receptors on RBC membranes[25]. This platform has preliminarily demonstrated its potent toxin neutralization ability on α-hemolysin secreted by *S. aureus*, but its broad-spectrum detoxification effect and related mechanisms is still not known.

Herein, the broad-spectrum detoxification effect of the hybrid nanovesicle, erythroliposome, was further assessed both *in vitro* in RBCs and *in vivo* in mice subcutaneously and intravenously challenged by three model PFTs, including α-haemolysin (Hlα), listeriolysin O (LLO) and streptolysin O (SLO) secreted by *S. aureus*, *Listeria monocytogenes*, and *Streptococcus pyogenes*, respectively (Fig. 1B). As RBC adherence of immune complexes containing toxins, virus, or bacteria could enhance macrophage uptake and facilitate the clearance from the circulation[26,27], we suppose that erythroliposomes composed of RBC membranes and lipid membranes may home to macrophages in the liver and the spleen for lysis after capturing PFTs, which helps PFT detoxification. Therefore, the *in vivo* behavior and the intracellular fate of erythroliposomes holding PFTs was firstly carefully investigated to clearly elucidate the underlying mechanisms of the extremely effective toxin detoxification capacity of erythroliposome using Hlα as a model PFT.

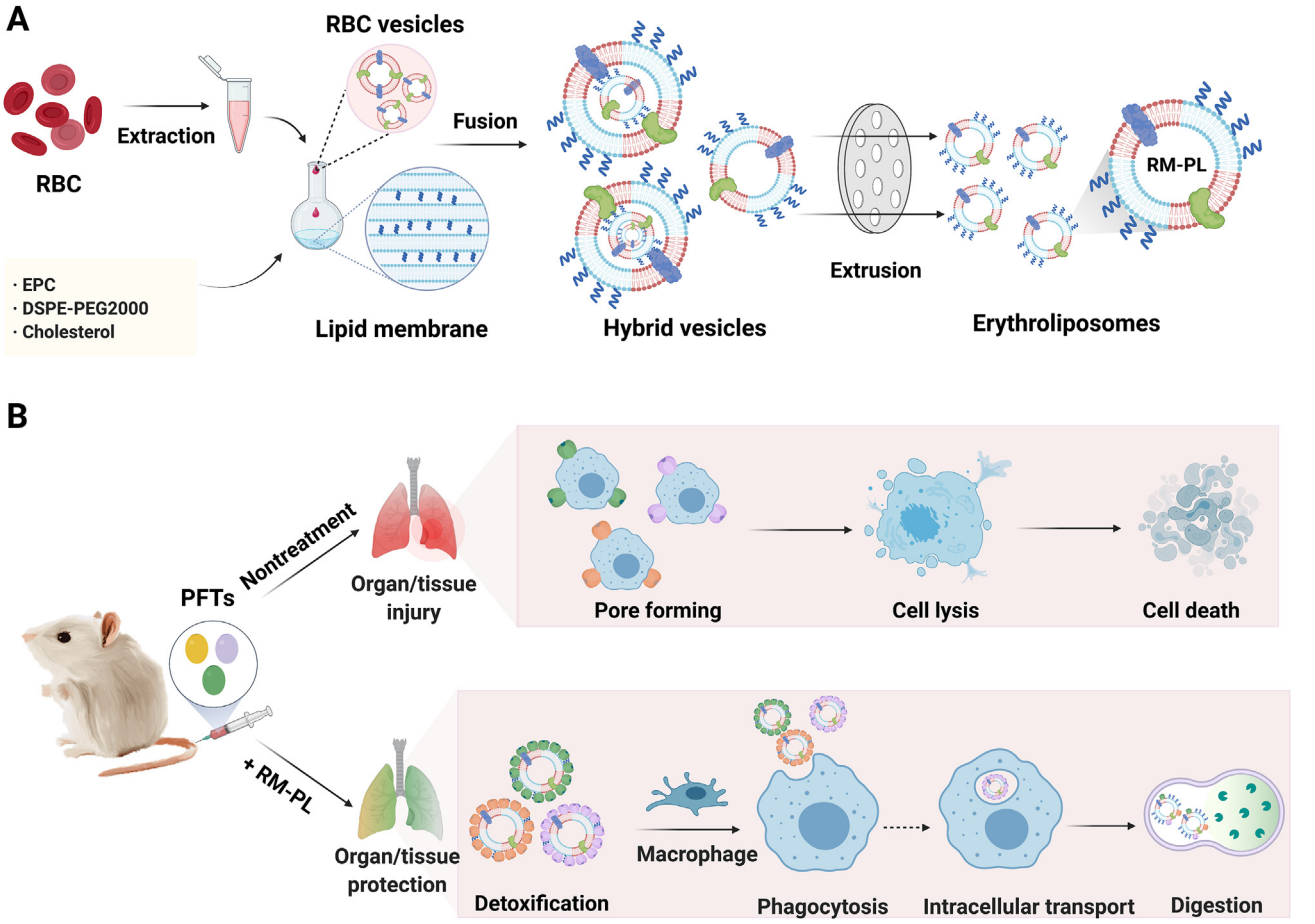

Figure 1 Broad-spectrum and powerful neutralization of bacterial toxins with erythroliposomes (RM-PL). (A) Schematics of preparation process of erythroliposomes. (B) The proposed mechanism of erythroliposomes to achieve broad-spectrum and powerful detoxification of bacterial toxins.

2. Materials and methods

2.1. Materials

Cholesterol, chlorpromazine, cytochalasin D, genistein, and methyl-β-cyclodextrin (mβCD) were obtained from Aladdin Biochem Technology Co., Ltd. (Shanghai, China). 1,1′-Dioctadecyl-3,3,3′,3′-tetramethylindodicarbocyanine, 4-chlorobenzen esulfonate salt (DiD), 2-(4-amidinophenyl)-6-indolecarbamidine dihydrochloride (DAPI), anti-fade mounting medium, blocking buffer for immunol staining and recombinant streptolysin O (SLO) were purchased from Beyotime (Haimen, China). RBC lysis buffer was obtained from MultiSciences Biotech (Shanghai, China). Amiloride was obtained from Solarbio Life Sciences Co., Ltd. (Beijing, China). Recombinant listeria monocytogenes Listeriolysin (LLO) protein was purchased from Abcam (Cambridge, UK). Collagenase IV, α-heamolysin (Hlα), and fluorescence tracker coumarin 6 were purchased from Sigma−Aldrich (ST. Louis, MO, USA). Anti-F4/80-FITC, anti-CD11c-FITC, anti-CD11b-Pacific Blue, anti-NK1.1-BV421, anti-CD49b-PE, anti-CD3-FITC, anti-CD19-FITC, anti-CD31-PE and anti-F4/80-AF488 were obtained from Biolegend (CA, USA). Egg yolk phosphatidylcholine (EPC) and *N*-(Carbonyl-methoxypolyethylene glycol 2000)-1,2-distearoyl-*sn*-glycerol-3-phosphoethanolamine (mPEG2000-DSPE) were purchased from AVT Pharmaceutical Tech Co., Ltd. (Shanghai, China). Serum-free cell freezing medium was purchased from Absin (Shanghai, China). Fetal bovine serum (FBS), DMEM medium, and penicillin−streptomycin were purchased from Gibco (Carlsbad, CA, USA).

RAW 264.7 cells were obtained from Chinese Academy of Science Cell Bank (Shanghai, China) and cultured in DMEM containing 10% FBS (*v*/*v*), 100 mg/mL streptomycin and 100 U/mL penicillin under standard condition. Male ICR mice (6 to 8 weeks old) were from the SinoBritish SIPPR/BK Lab Animal (Shanghai, China). All experiments were carried out according to the protocol approved by the Ethics Committee of Fudan University (Approval code: 2017-03-YJ-PZQ-01).

2.2. RBC membrane derivation

The RBC membrane was derived from the whole blood based on previously described protocols with modifications[22]. Briefly, RBCs were collected from 1 mL of anticoagulated whole blood of ICR mice by centrifugation at 700×*g* for 5 min at 4 °C. The pellet was washed with ice-cold 1 × PBS containing 1 mmol/L EDTA three times to purify RBCs and then suspended in 0.2 mmol/L EDTA solution for hemolysis. Lysed cells were centrifuged at 20,000×*g* for 10 min at 4 °C for hemoglobin removal. The supernatant was discarded, and the resulting pellet was further purified with 0.2 mmol/L EDTA solution. The RBC membranes were finally collected as pink pellets, suspended in 1 mL of 0.2 mmol/L EDTA solution and stored at −80 °C for subsequent use.

2.3. Preparation of RM-PL

RM-PL was prepared by a thin-film hydration and extrusion method in accordance with previously reported protocols with modifications[25]. Briefly, 2.0 mg of EPC, 1.6 mg of cholesterol and 0.4 mg of mPEG2000-DSPE were dissolved in 3 mL of dichloromethane, and the solvent was then evaporated in a round flask through a rotary evaporator (Rotavapor R100, Buchi, Switzerland) to form a thin film. The lipid film was hydrated with 1.85 mL of double-distilled H_2O and 150 μL of RBC membrane suspension or with 2 mL of double-distilled H_2O to prepare RM-PL or conventional PEGylated liposomes (PL). Next, the suspension was sonicated in ice-cold water for 4 min using a bath sonicator and then extruded through 0.2 and 0.1 μm polycarbonate membranes (Nuclepore Track-Etched Membranes, Whatman, UK) using a LiposoFast extruder apparatus (Avestin, LF-1, Canada). The resulting RM-PL was stored at 4 °C until use. To prepare RMV of a comparable size, the RBC membrane suspension suspended in 0.2 mmol/L EDTA solution was directly sonicated in ice-cold water for 4 min followed by extrusion through 0.2 and 0.1 μm polycarbonate membranes. For fluorescence microscopy imaging and *in vivo* particle tracking purposes, DiD-labelled RM-PL was prepared as described above except that 8 μg of DiD was added to the lipids prior to the thin film formation.

2.4. Membrane fusion verification

The fusion of RBC membranes and lipid membranes was verified by the membrane colocalization study as previously described[28]. In brief, RBC membranes were labeled with coumarin 6, (excitation/emission = 466/504 nm), and lipid membranes were labeled with DiD (excitation/emission = 640/670 nm). RM-PL was prepared as described above using these dye-labeled membranes and was then visualized under a confocal fluorescence microscope (Nikon N-SIM, Japan) at 1000 × magnification. It should be noted that in order to see nanovesicles clearly under the microscope, RM-PL was only passed through 1 μm polycarbonate membranes repeatedly.

2.5. Characterization of RM-PL

The structure and morphology of the RM-PL were visualized using both transmission electron microscope (TEM) and cryogenic electron microscopy (Cryo-EM). For TEM imaging, RM-PL at a concentration of 0.1 mg/mL was deposited onto a glow-discharged carbon-coated grid and was then stained with 1% uranyl acetate. The grid was dried at room temperature and visualized using a TECNAI G2 S-TWIN microscope (FEI, USA). For Cryo-EM imaging, RM-PL was plunge-frozen on holey film grids. A 626 cryo-specimen holder was used for imaging. Data were collected on a JEOL 2100 electron microscope (Japan). Images were recorded under low electron dose conditions (5−20 electron/Å2) using a 4096 × 4096 pixel CCD camera (UltraScan 895, GATAN, Inc., Pleasanton, CA, USA) at a nominal magnification of 20,000 × .

A dynamic light scattering (DLS) detector (Zetasizer, Nano-ZS, Malvern, UK) was employed to measure the size, polydispersity index, and ζ potential of RM-PL. Samples were diluted 20 folds with distilled water at room temperature. The measurements were performed in triplicate. To examine the stability of the formulations in solution, RM-PL was suspended in 1 × PBS or PBS containing 5% fetal bovine serum (FBS) at 4 °C at a concentration of 2 mg/mL. The particle size and polydispersity index were monitored by DLS daily for 6 or 5 days.

2.6. Quantification of toxin hemolytic activity

The hemolytic activity of toxins was tested as previously described[23]. Briefly, serial dilutions of bacterial toxins (60 μL) were added to 100 μL of 5% (*v*/*v*) purified mouse RBCs, and the mixture was incubated at 37 °C for 3 h. Following the incubation, cells were spun down by centrifugation at 3000 rpm for 10 min (Thermo Fisher Tx-400, USA) and the concentration of released hemoglobin in the supernatant was quantified by measuring the absorbance at 540 nm using a plate reader (TECAN M1000, USA). The relative hemolysis was determined by comparing the absorbance with that of the RBC samples disrupted with 2% (*v*/*v*) Triton X-100, using the following Eq. (1):

$$\text{Relative hemolysis (\%)} = (OD540_{sample} - OD540_{PBS}) / (OD540_{Triton} - OD540_{PBS}) \times 100 \quad (1)$$

In this experiment, if the relative hemolysis exceeds 100%, which means the toxin disrupted RBCs more seriously than Triton X-100, it is set to 100%. In the study, hemolysis dosage 100% (HD100) was defined as the minimum toxin concentration that induced 100% hemolysis.

2.7. Toxin neutralization of PFTs by RM-PL in vitro

To qualitatively determine the ability of RM-PL to neutralize toxins, a hemolysis assay was first performed in Eppendorf tubes. Hlα (2 μg) was incubated with RM-PL (10 μg) for 30 min, and the mixture was then added with fresh 5% RBCs (1.8 mL), followed by incubation for 3 h at 37 °C. The RBC hemolysis was imaged and the relative hemolysis was determined as described above. PBS without toxin, Triton X-100 without toxin, PBS, PL with equal lipid mass to RM-PL, and RMV with equal RBC membranes to RM-PL were tested in parallel as controls.

In vitro toxin neutralization ability of RM-PL was then examined as previously described[23]. Briefly, different amounts of RM-PL was added to toxins of HD100 and incubated for 30 min at room temperature (The total volume was 60 μL). Then 100 μL of 5% purified mouse RBCs were added. The mixture was incubated for an additional 3 h at 37 °C prior to hemolysis quantification. The minimum RM-PL concentration that completely inhibited toxin hemolysis was defined as the inhibitory concentration 100% (IC100). RBC samples either without any treatment or simply subjected to toxins alone were used as negative and positive controls, respectively. All experiments were performed in triplicate.

2.8. In vivo detoxification of PFTs by RM-PL following subcutaneous challenge

Six week-old male ICR mice were randomly divided into three groups. For the detoxification group, RM-PL was incubated with each toxin at the dose ratio of IC100 to HD100 for 30 min at room temperature, and the mixture was then injected subcutaneously into the hind legs of the mice. Mice received free toxins without RM-PL served as positive controls. For negative control, equal volume of PBS was injected. The injection region was photographed and the lesion area was recorded daily. At 3 days after injection, the mice were sacrificed, and the skin and muscle samples at the injection site were collected for hematoxylin−eosin (H&E) staining.

2.9. *In vivo detoxification of PFTs by RM-PL following intravenous challenge*

Six-week-old male ICR mice were randomly divided into two groups. The mice were intravenously injected with each toxin of a lethal dose followed by an injection of RM-PL (the dose ratio of RM-PL to toxin was IC100: HD100) or PBS 2 min later. The survival of mice after injection was recorded, and the statistical significance was analyzed using the log-rank test. The mice survived in detoxification treatment were sacrificed at 6 and 24 h after injection and their major organs including the heart, the liver, the spleen, the lung, and the kidney were collected, while the major organs of mice died of toxins were immediately removed after their death. Major organs were then fixed in 4% paraformaldehyde, embedded in paraffin, sectioned, and examined with regards to gross pathology and histology by H&E staining.

2.10. *Pharmacokinetics and biodistribution of RM-PL absorbing Hlα*

To investigate the *in vivo* behavior of RM-PL absorbing toxins, the pharmacokinetics and biodistribution of RM-PL absorbing Hlα or not using Hlα as a model PFT was studied. In brief, RM-PL absorbing toxins (RM-PL+Hlα) were prepared by incubation of 200 μg of RM-PL and 5 μg of Hlα as described above. Male ICR mice aged six weeks were randomly divided in three groups and intravenously injected with 200 μg of DiD-labeled RM-PL (100 μL), DiD-labeled RM-PL+Hlα (100 μL), and 5 μg of Hlα followed by 200 μg of DiD-labeled RM-PL (100 μL) 2 min after Hlα injection [RM-PL(Hlα)], respectively. Blood samples were collected at different time points (1, 5, 15, and 30 min; 1, 2, 4, 6, 8, 12, and 24 h) *via* cheek pouch puncture, and the fluorescence intensity of the blood was measured with on a plate reader (TECAN M1000, USA) at the excitation wavelength of 640 nm and the emission wavelength of 670 nm. Statistical moment theory was applied to determine the pharmacokinetic parameters of these nanovesicles including area under the concentration−time curve (AUC), mean residence time (MRT), clearance (Cl), and half-life ($t_{1/2}$). To study the biodistribution of the different formulations, the mice were sacrificed 24 h after injection and perfused with PBS. Major organs, including the heart, liver, spleen, lung, brain and kidney, were collected, weighed, homogenized in PBS, and analyzed on a plate reader (TECAN M1000, USA) to determine the fluorescence intensity.

2.11. *Identification of cellular phenotype taking up RM-PL absorbing Hlα*

RM-PL+Hlα was prepared by incubation of 200 μg of DiD-labeled RM-PL and 5 μg of Hlα as described above and then injected into 6-week-old ICR mice. The mice were sacrificed 18 h later, and their livers and spleens were collected for flow cytometry analysis. To isolate splenocytes, spleen was cut, mashed and passed through a 70 μm cell strainer. Cells were collected by centrifugation at 800×*g* for 3 min at 4 °C, resuspended in 1 mL of RBC lysis buffer to remove RBCs, and washed with PBS. Splenocytes were then analyzed by flow cytometry (Beckman, CA, USA) after staining with cell type specific markers ($CD3^+$ T cells, $CD19^+$ B cells, $NK1.1^+CD49b^+$ NK cells, $F4/80^+$ macrophages, $CD11b^+$ $F4/80^-$ monocytes, and $CD11c^+$ DCs). To isolate liver cells, the liver was placed in a sterile Petri dish containing 3 mL of the digest solution (0.2 mg/mL collagenase IV in RPMI1640 medium), cut into small pieces, and incubated at 37 °C for 60 min to release cells into the solution. The suspension was filtered through a 70 μm cell strainer to remove undigested and connective tissues, centrifuged at 375×*g* for 5 min at 4 °C, and resuspended

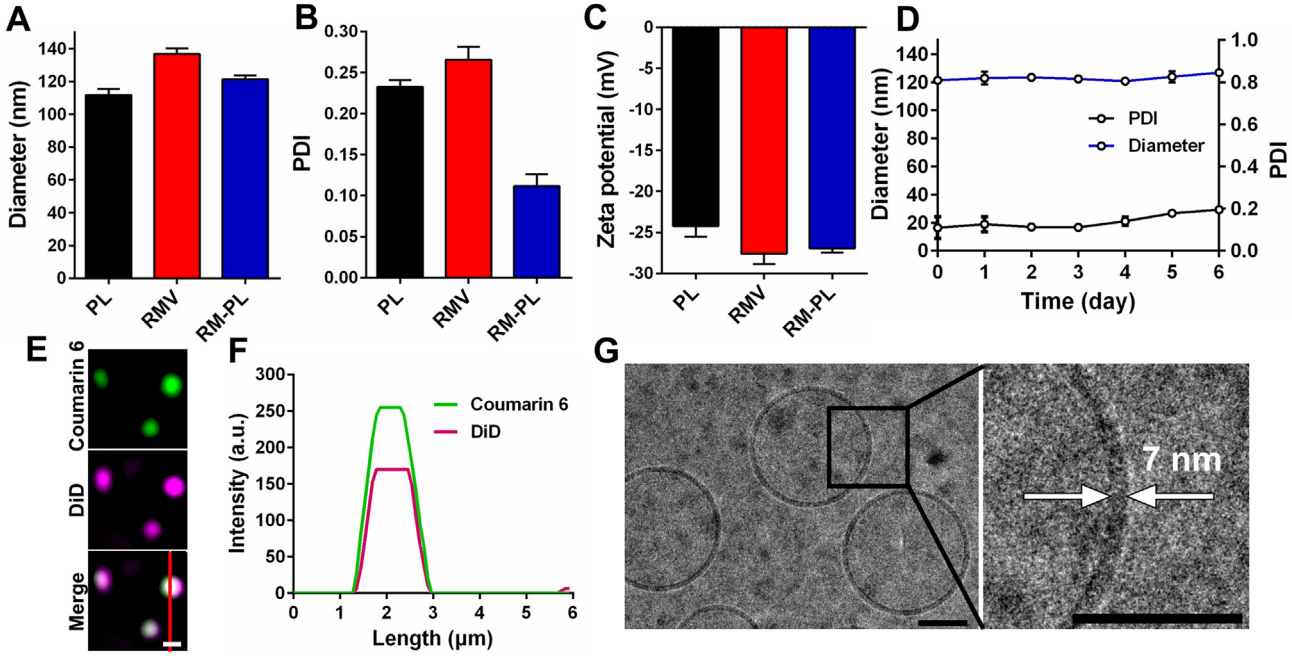

Figure 2 Preparation and characterization of RM-PL. (A) Diameter, (B) polydispersity index (PDI), and (C) zeta potential of PL, RMV, and RM-PL (mean ± SD, $n = 3$). (D) Long-term stability of RM-PL in PBS monitored over 6 days (mean ± SD, $n = 3$). (E) Confocal fluorescence images of RM-PL and (F) the corresponding fluorescence intensity profiles along the red line crossing the representative RM-PL. Green, RBC membranes; Purple, lipid membranes; scale bar = 1 μm. (G) Representative cryogenic electron microscopy (Cyro-EM) image of RM-PL (left) and the enlarged image of the RM-PL membrane (right); scale bar = 50 nm.

with 2 mL of FACs (fluorescence-activated cell sorter) buffer. Cell suspensions from the liver were then stained with cell type specific markers ($CD19^+$ B cells, $CD3^+$ T cells, $CD31^+$ endothelial cells, $F4/80^+$ kupffer cells) and analyzed by flow cytometry (Beckman, CA, USA).

2.12. *Immunofluorescence staining of cells taking up RM-PL absorbing Hlα*

The livers and spleens of mice injected with RM-PL+Hlα were collected for immunofluorescence study. Seven-μm-thick frozen tissue sections were cut using Cryostat (Leica CM3050S), mounted on Superfrost Plus slides (Fisher Scientific Co., Houston, TX, USA), and stored in a −70 °C freezer. Before staining, slides were allowed to air dry at room temperature for 10 min. After washing with 1 × PBS, sections were incubated for 30 min at room temperature in blocking buffer. Sections of spleens or livers were then incubated with 5 μg/mL of anti-F4/80 antibody conjugated with Alexa 488 for 1 h at room temperature. After washing in PBS, sections were counterstained with DAPI (1 μg/mL) and mounted with anti-fade mounting medium. The slides were visualized under a confocal fluorescence microscope (ZEISS, 710, LSM, wetzlar, Germany).

2.13. *Cellular uptake of RM-PL absorbing Hlα*

For cellular internalization observation, RAW 264.7 cells were seeded into a laser confocal Petri dish at a density of 2×10^5 cells per well and were cultured for 24 h at 37 °C in a 5% CO_2 atmosphere. The cells were washed with PBS and subsequently treated with 0.8 mg/mL of DiD-labeled RM-PL+Hlα. After 4 h incubation, the cells were washed with PBS to remove the medium and free nanovesicles. After incubation with 4% paraformaldehyde for 15 min at room temperature, cells were stained with DAPI for 10 min and washed with PBS. The dishes were imaged with a fluorescence microscopy (ZEISS, 710, LSM, Germany).

Endocytosis inhibition experiments were performed on RAW 264.7 cells to investigate the cellular internalization mechanism of RM-PL+Hlα by macrophages. RAW 264.7 cells were seeded in 12-well plates at the density of 2×10^5 cells per well and cultured for 24 h. After that, RAW 264.7 cells were preincubated with different endocytic inhibitors including 6.5 mg/mL of methyl-β-cyclodextrin (M-β-CD), 1.5 mg/mL of amiloride, 5 μg/mL of cytochalasin D, 0.1 mg/mL of genistein, 5 μg/mL of chlorpromazine, and 0.1 mol/L of chloroquine phosphate for 30 min at 37 °C, respectively, or pretreated at 4 °C for 30 min. Then, RM-PL+Hlα was added at the RM-PL concentration of 0.8 mg/mL and incubated for another 4 h. Afterward, RAW 264.7 cells were harvested, washed with PBS and analyzed by flow cytometry (Beckman, CA, USA).

2.14. *Intracellular trafficking of RM-PL+Hlα in macrophages*

To visualize intracellular distribution of RM-PL absorbing toxin, RAW 264.7 cells were incubated with 0.8 mg/mL of DiD-labeled

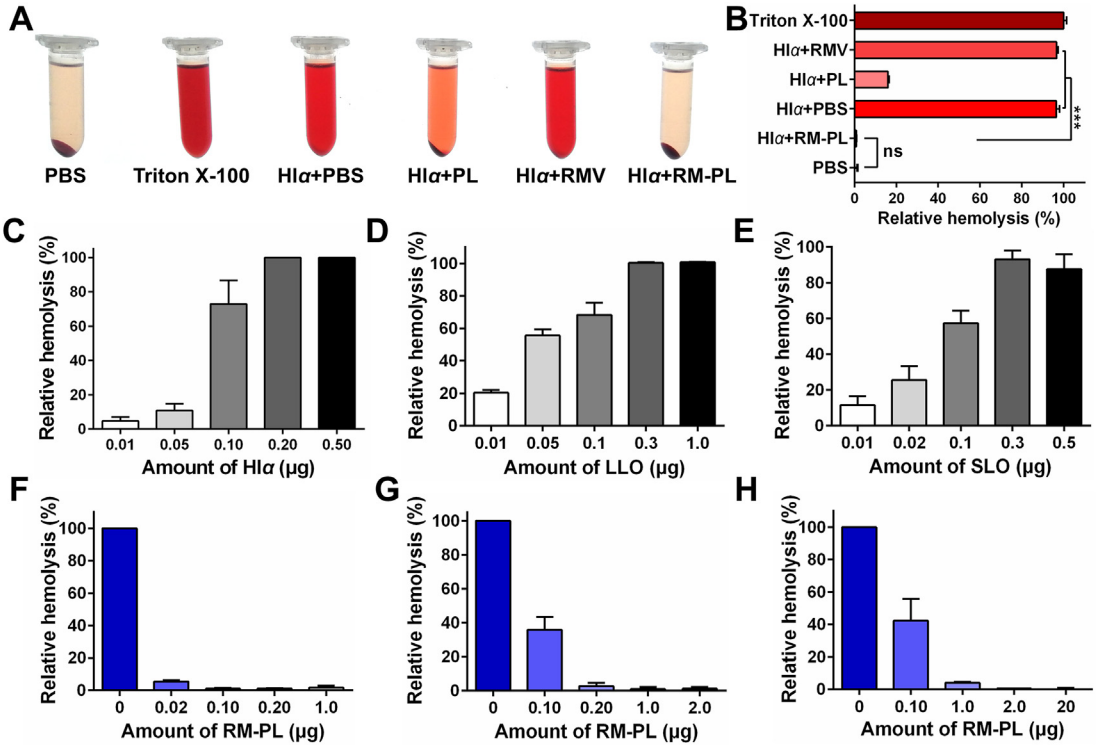

Figure 3 Broad-spectrum PFT neutralization capability of RM-PL *in vitro*. (A) Images of RBC hemolysis after RBCs were incubated with Hlα treated with saline, PL, RMV, or RM-PL and (B) the corresponding relative hemolysis (mean ± SD, $n = 3$). PBS without Hlα and Triton X-100 without Hlα were used as the negative and positive controls, respectively. ***$P < 0.0001$, compared with Hlα+RM-PL. (C−E) Hemolytic activity of free (C) Hlα, (D) LLO and (E) SLO on 5% mouse RBC *in vitro*. (F−H) Dose-dependent PFT neutralization of RM-PL against (F) Hlα, (G) LLO and (H) SLO determined through RBC hemolysis.

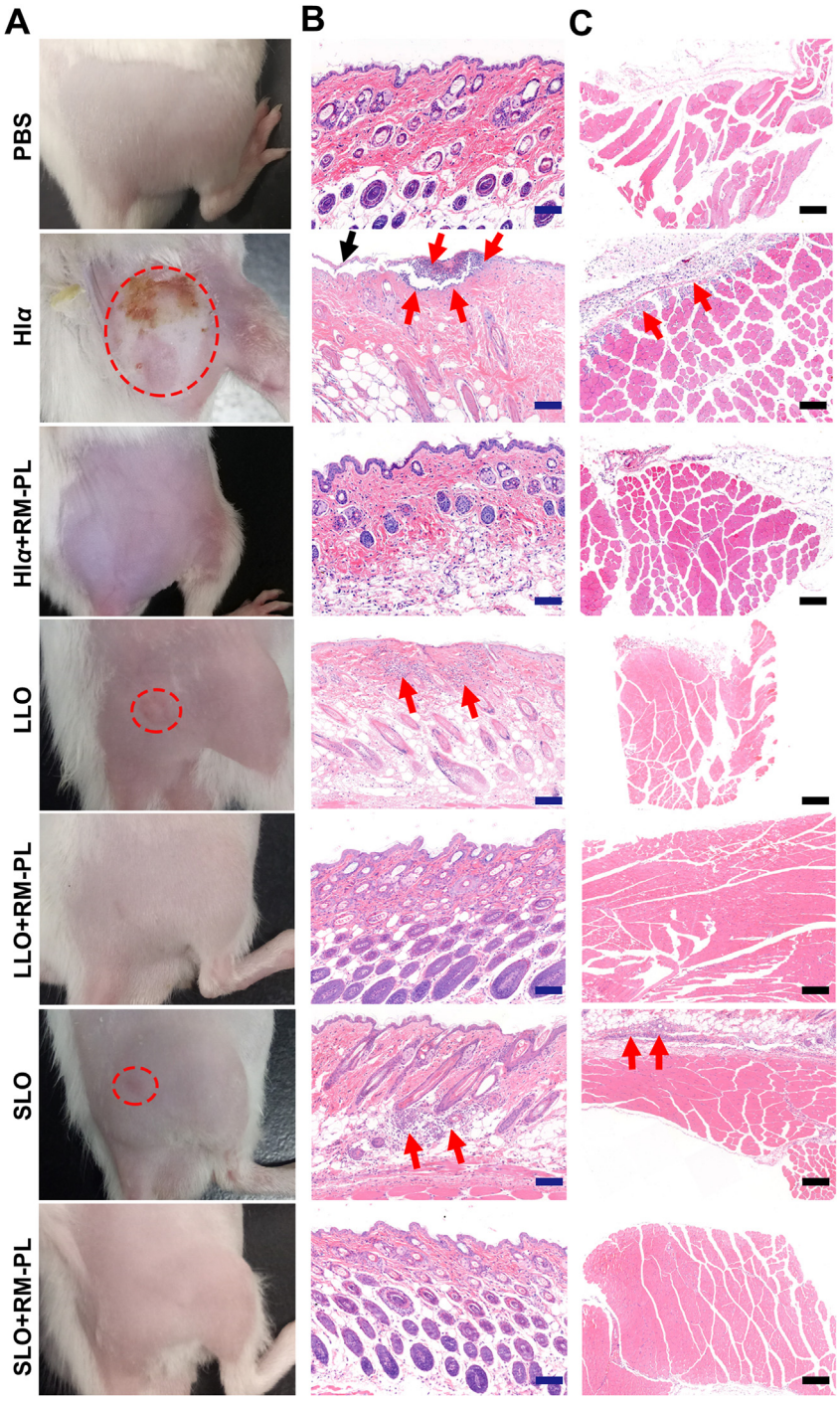

Figure 4 *In vivo* detoxification of PFTs by RM-PL following subcutaneous challenge. (A) Images of skin lesions occurred 3 days post injection. The red dotted circle indicated the lesion area. (B, C) The haematoxylin and eosin (H&E)-stained histological sections of (B) skin and (C) conjoint muscle samples at the injection site 3 days post injection. The black arrow indicated the damaged skin epidermis. The red arrow indicated the infiltration of inflammatory cells. Scale bar = 200 μm. Normal mice without PFTs challenge was treated with PBS and served as a control.

RM-PL+Hlα for 0.5, 2, 4, 6 and 24 h, respectively. Then, cells were collected and washed with PBS to remove free nanovesicles. LysoGreen (1 μmol/L) was added to cells and incubated for another 30 min to label lysosomes. Afterward, cells were washed with PBS, fixed with 4% formaldehyde for 15 min, and stained with 2 μg/mL of DAPI. Then cells were visualized under a confocal fluorescence microscope (ZEISS, 710, LSM, Wetzlar, Germany) and the colocalization of RM-PL+Hlα and lysosomes was analyzed with ImageJ software.

2.15. *Statistical analysis*

Unpaired Student's *t*-test was used for statistical analyses. All data were presented as mean ± standard deviation (SD).

Statistical differences were defined as $^{*}P < 0.05$, $^{**}P < 0.01$, and $^{***}P < 0.001$.

3. Results and discussions

3.1. Preparation and characterization of RM-PL

RM-PL was prepared by the conventional thin-film hydration and extrusion method, as shown in Fig. 1A. Firstly, RBC membranes were obtained by the hypotonic method. Secondly, lipid membranes were prepared using EPC with a low phase transition temperature and cholesterol as the main components. Finally, lipid membranes were fused with RBC membranes by sonication and extrusion. The addition of artificial lipid material into RBC membranes can modulate the structural fluidity of the natural cell membrane, which particularly benefits the fusion process. The pure RBC membrane was difficult to extrude through the polycarbonate membranes, but the procedure became much easier after fusion with the artificial lipid membrane. Cholesterol has been known as a key component of animal cell biological membranes, modulating the membrane elasticity, the packing density of lipids, and the formation of lipid rafts[29,30]. Moreover, a family of PFTs called cholesterol-dependent cytolysins (CDCs) use cholesterol as a major receptor during pore formation[10,31] and cholesterol added in RM-PL might increase the CDC neutralization ability of RM-PL. In the present study, RBC and lipid membranes were fused at an RBC membrane: lipid membrane surface area ratio of 1:23 (Supporting Information), indicating that most of the surface area of the RM-PL was covered by the artificial lipid membrane. In addition, mPEG2000-DSPE was added to enhance the stability of RM-PL *in vitro* and *in vivo*. The mixture of RBC membranes and artificial lipid membranes was physically extruded through polycarbonate membranes to facilitate cell membrane-lipid membrane fusion with little damage to cell membrane components.

As measured by DLS, the average size of PL and RM-PL was approximately 120 nm with a narrow size distribution, while RMV were relatively larger (Fig. 2A, B), possibly due to the mechanical rigidity of pure RBC membranes. After fusion with artificial lipid membranes, RBC membranes became more flexible and easier to form into smaller nanovesicles. Moreover, the ζ potential value of RM-PL was between that of RMV and PL (Fig. 2C), suggesting the successful fusion of RBC membranes with liposomal membranes. To examine the stability of RM-PL, samples were diluted with PBS or PBS containing 5% fetal bovine serum and stored at 4 °C. The size and polydispersity index (PDI) of RM-PL remained stable throughout the whole study (Fig. 2D and Supporting Information Fig. S1), suggesting that RBC membrane fusion did not influence the stability of liposomal structures.

Next, the fusion of lipid membranes and RBC membranes in RM-PL was further visualized *via* a confocal fluorescence microscopy (Fig. 2E, F). It was shown that the purple fluorescence of lipid membranes was clearly overlaid with the green fluorescence of RBC membranes, indicating the successful fusion of lipid membranes and RBC membranes.

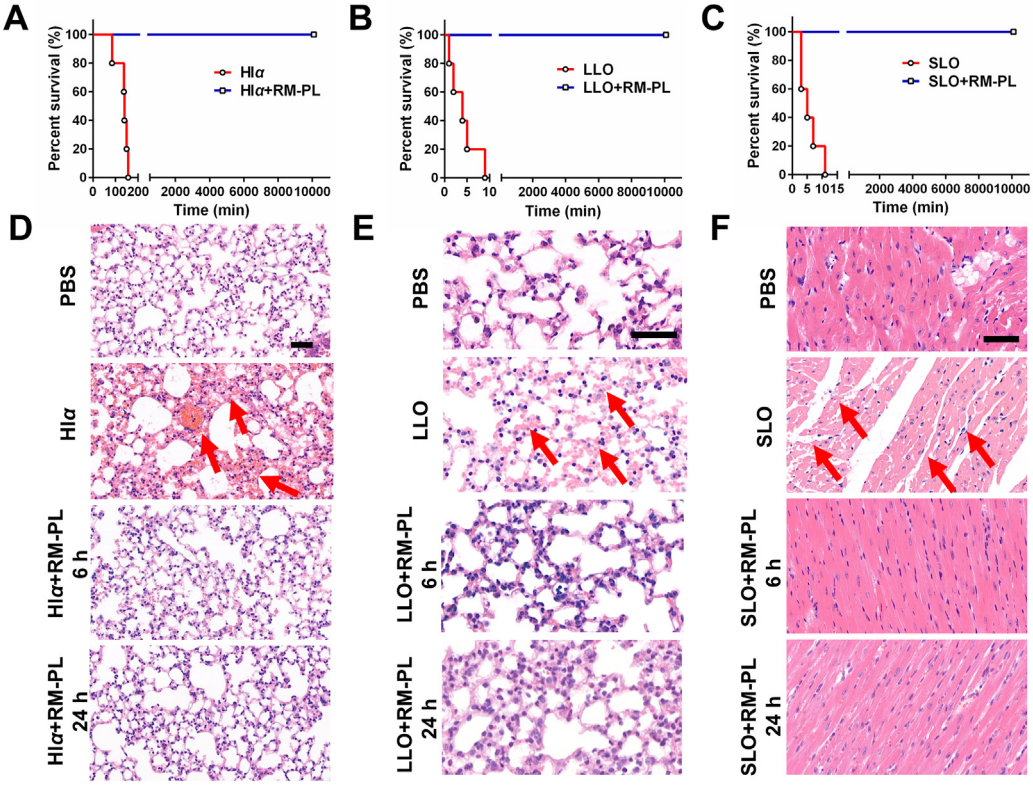

Figure 5 *In vivo* detoxification of PFTs by RM-PL following intravenous toxin challenge. (A–C) Survival curves of mice treated with an intravenous injection of RM-PL 2 min after the injection of a lethal dose of (A) Hlα, (B) LLO and (C) SLO ($n = 5$). (D, E) The H&E stained slices of the lung from mice treated with RM-PL after intravenous (D) Hlα and (E) LLO challenge, respectively. (F) The H&E stained slices of the heart from mice treated with RM-PL after intravenous SLO challenge. Scale bar = 50 μm. Normal mice without intravenous toxin challenge was treated with PBS and served as a control.

TEM and cryo-TEM images revealed that RM-PL had a spherical vesicular structure with a diameter of approximately 120 nm (Fig. 2G and Supporting Information Fig. S2). Closer examination revealed that the membrane thickness of RM-PL was approximately 7−8 nm (Fig. 2G and Fig. S2), which was in agreement with that of RBCs (∼7.5 nm)[32,33] but higher than that of liposomes (3.4−4.4 nm)[34], further suggesting the successful membrane fusion of lipid membranes and RBC membranes.

3.2. *In vitro neutralization of PFTs with RM-PL*

To qualitatively determine the ability of RM-PL to neutralize toxins, a hemolysis assay was performed in Eppendorf tubes using Hlα as a model PFT. As shown in Fig. 3A, only the RM-PL group showed a clear supernatant similar to that of the negative control group (PBS without toxin), suggesting that RM-PL could neutralize the hemolytic activity of Hlα and RBCs were protected from disruption. The supernatants of the other groups had a deep red color, while the sizes of the RBC pellets at the bottom of the Eppendorf tubes were significantly decreased compared with the HlαRM-PL group or the HlαPBS group. The relative hemolysis percentage results revealed that RM-PL could completely neutralize Hlα toxicity, while RMV did not neutralize Hlα and PL partly neutralized Hlα toxicity (Fig. 3B). These results suggest that lipid membranes fusion with RBC membranes could sharply amplify the toxin neutralization ability of RBC membranes.

We next examined the broad-spectrum toxin-neutralizing capacity of RM-PL. We choose three representative PFTs (Hlα, SLO and LLO) playing key roles in bacterial infections which threaten the public health and safety. First, to quantify the hemolytic activity of different PFTs against RBCs, serial amounts of PFTs were tested on 5% RBC suspension. The hemolysis percentage increased with PFT concentration, and finally reached a plateau (Fig. 3C−E). Based on the hemolysis measurements, ∼0.2 μg Hlα, 0.3 μg LLO and 0.3 μg SLO caused complete lysis of 100 μL of 5% (*v*/*v*) RBCs (Fig. 3C−E).

Then, the capacity of RM-PL to neutralize these three PFTs was tested (Fig. 3F−H). It was found that the detoxification capability of RM-PL was dose-dependent and PFT type-dependent. Based on the hemolysis results, 0.1 μg of RM-PL could neutralize 0.2 μg of Hlα, 1.0 μg of RM-PL could neutralize 0.3 μg of LLO, and 2.0 μg of RM-PL could neutralize 0.3 μg of SLO (Fig. 3F−H). To further confirm the presence of PFTs on RM-PL after incubation, a dot blot assay was performed using Hlα as a model PFT. The blot intensities revealed that around 93% of Hlα was sponged on RM-PL after incubation for 30 min, suggesting that most toxins were quickly sponged to RM-PL and was difficult to release from RM-PL in 30 min (Supporting Information Fig. S3). In the present study, RBC membranes and lipid membranes were fused at the RBC membrane and lipid membrane surface area ratio of 1:23 (Supporting Information). This means that one single red blood cell could be used to prepare more nano-antidotes (RM-PL) compared with nanosponges which were totally wrapped by RBC membranes. As a result, the likelihood of interactions between toxins and RM-PL is increased. Meanwhile, the lipid membrane in RM-PL provides larger room for PFT insertion compared with nanosponges. It was estimated each RM-PL could neutralize 3430 Hlα molecules, and RM-PL

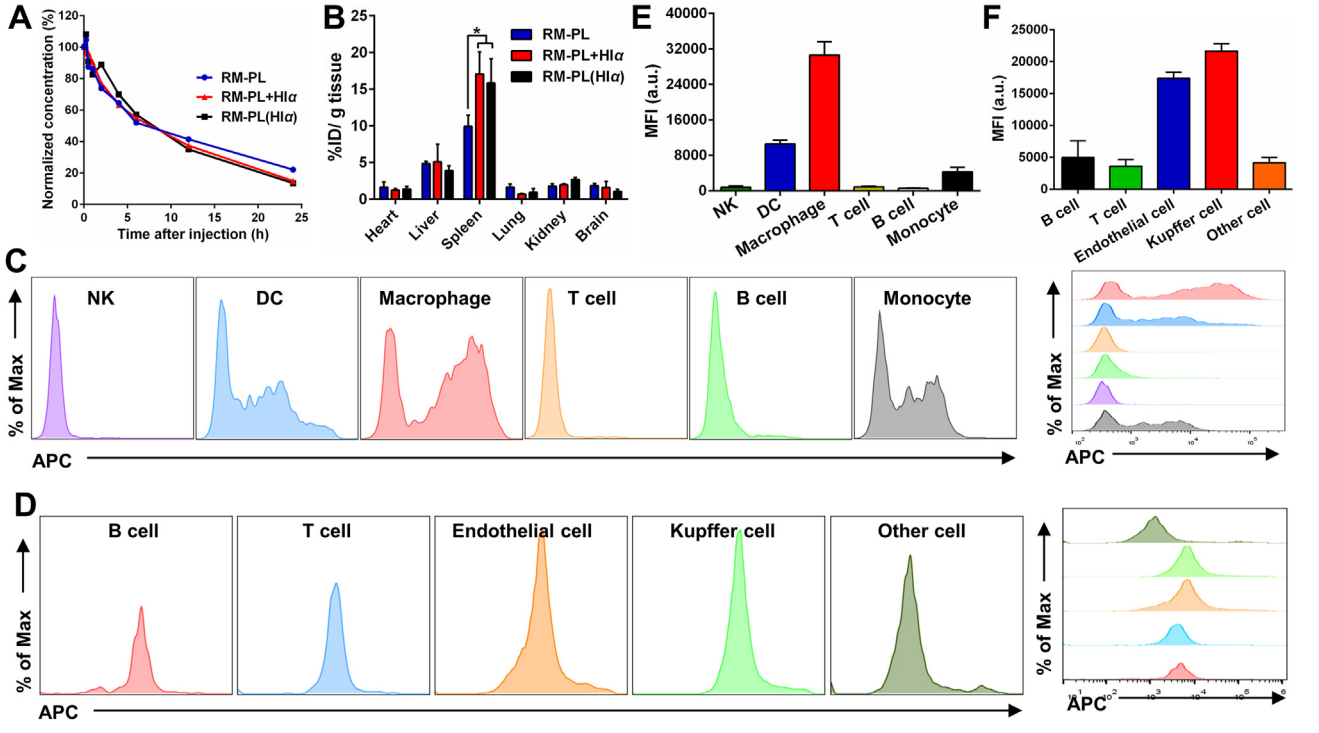

Figure 6 *In vivo* fate of RM-PL+Hlα after intravenous injection. (A) Circulation profiles of RM-PL+Hlα after intravenous injection ($n = 4$). (B) Biodistribution of RM-PL+Hlα at 24 h after intravenous injection (mean ± SD, $n = 4$). *$P < 0.05$, compared with RM-PL. (C) Flow histograms of different types of splenic cells internalized DiD-labeled RM-PL+Hlα. (D) Flow histograms of different types of liver cells internalizing DiD-labeled RM-PL+Hlα. (E, F) The corresponding mean fluorescence intensity (MFI) of different cells (E) in the spleen and (F) in the liver internalizing DiD-labeled RM-PL+Hlα (mean ± SD, $n = 4$).

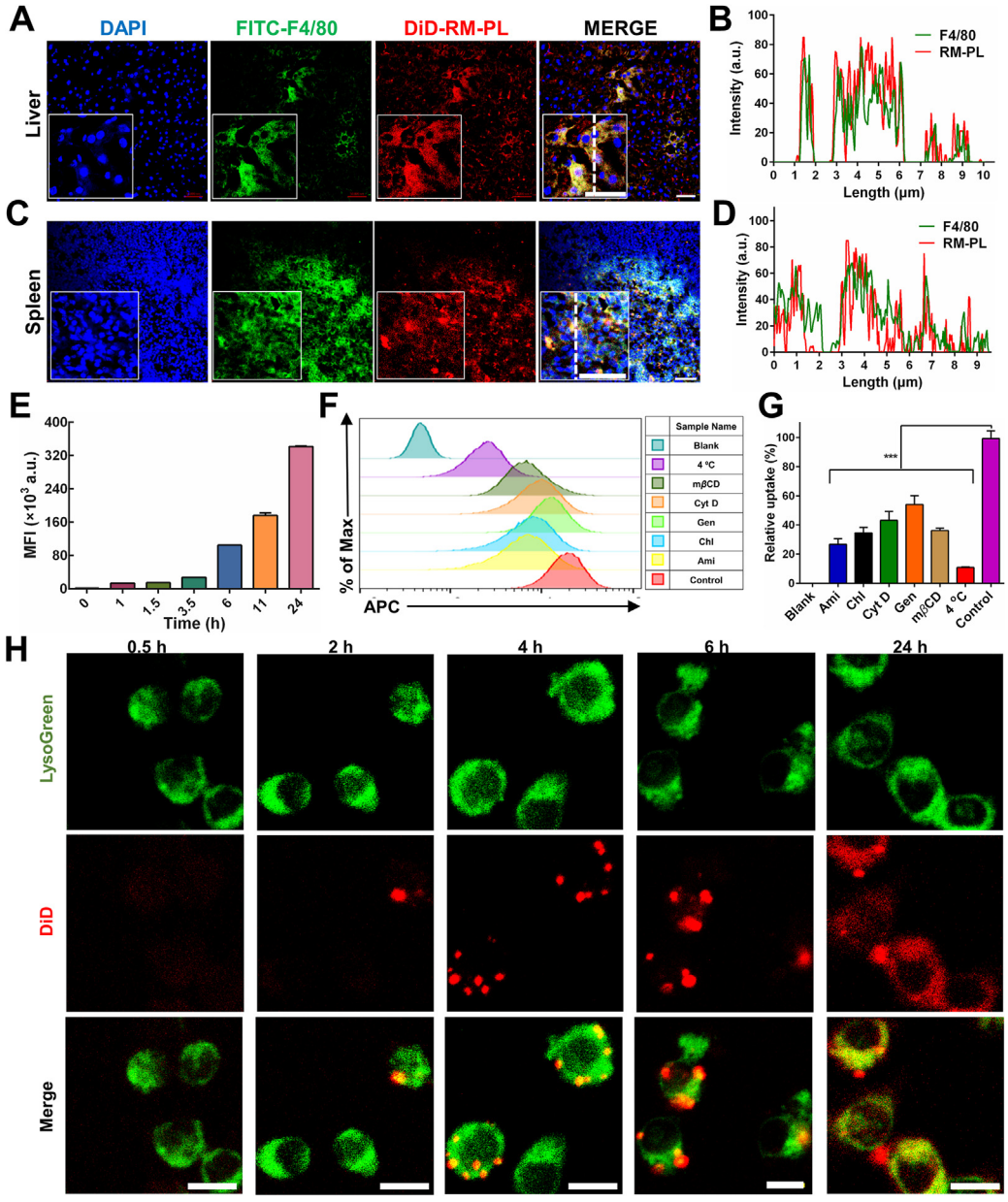

Figure 7 Cellular uptake of RM-PL+Hlα. (A) Confocal fluorescence microscopy images demonstrating the location of DiD-labeled RM-PL+Hlα in the liver kupffer cells and (B) the corresponding fluorescence intensity profiles of RM-PL and kupffer cells along the dotted white line. (C) Confocal fluorescence microscopy images demonstrating the location of DiD-labeled RM-PL+Hlα in the spleen macrophages and (D) the corresponding fluorescence intensity profiles of RM-PL and macrophages along the dotted white line. Sections were stained with anti-F4/80-FITC (green) and counterstained with DAPI (blue). Scale bar = 5 μm. (E) The mean fluorescence intensity (MFI) of cells obtained by flow cytometry was plotted with time, demonstrating time-dependent cellular uptake profiles of DiD-labeled RM-PL+Hlα by RAW264.7 cells. (F) Flow cytometry analysis and (G) the corresponding quantitative results for cellular uptake of DiD-labeled RM-PL+Hlα by RAW 264.7 cells in the presence of different endocytosis inhibitors (mean ± SD, n = 3). Ami, amiloride; Chl, chlorpromazine; Cyt D, cytochalasin D; Gen, genistein. Cells treated with DiD-labeled RM-PL+Hlα in the absence of endocytosis inhibitors were used as control and untreated cells were used as Blank. ***$P < 0.0001$, compared with Control. (H) Representative fluorescence images of RAW 264.7 cells incubated with DiD-labeled RM-PL+Hlα for 0.5, 2, 4, 6 and 24 h, respectively. Green, Lysosomes; Red, DiD-labeled RM-PL+Hlα. Scale bar = 10 μm.

made from one RBC could neutralize up to 1.95×10^8 Hlα molecules (Supporting Information), nearly 694-fold more than nanosponges made from one RBC (2.8×10^5 Hlα molecules)[35]. Additionally, the Hlα detoxification capability of RM-PL was increased compared with that of RM-PL without cholesterol (3.9×10^7 Hlα molecules)[25], indicating the addition of cholesterol, a receptor for some PFTs and a key component of lipid rafts in RM-PL helped the assembly and insertion of Hlα into RM-PL. Meanwhile, it was estimated each RM-PL could neutralize 270 SLO molecules or 325 LLO molecules, and RM-PL made from one RBC could neutralize up to 1.53×10^7 SLO molecules and 1.84×10^7 LLO molecules. The SLO neutralization capability of RM-PL made from one RBC was nearly 154-fold that of nanosponges made from one RBC. These results suggest that RM-PL

could not only neutralize different PFTs with extremely high efficiency but also greatly economize the natural membrane resources, holding great potential in antivirulence therapy.

3.3. *In vivo detoxification of PFTs by RM-PL following subcutaneous challenge*

PFT neutralization by RM-PL was first assessed *in vivo* by the subcutaneous injection of PFTs into the right flank region of ICR mice. Severe skin lesions with apparent irritation and trauma were observed in the Hlα group at 3 days after injection but not observed in the Hlα+RM-PL group (Fig. 4 and Supporting Information Fig. S4). Skin inflammation symptoms such as redness and swelling also appeared in the LLO and SLO groups after injection (Fig. 4, Supporting Information Figs. S5 and S6). Moreover, the lesion areas indicated no skin damage at the injection site in the detoxification groups (Supporting Information Fig. S7). As shown in Fig. 4, H&E-stained skin and muscle sections from the toxin group exhibited noticeable inflammatory cell infiltration and cell necrosis 3 days after injection. In contrast, no skin lesions were seen in the RM-PL treatment group, and the H&E-stained sections demonstrated normal and intact tissue structures, no inflammatory cell infiltration, and no cell necrosis. Further flow cytometry analysis of damaged skins and adjacent tissues revealed that significantly higher levels of inflammatory cells (including total leukocytes, macrophages, monocytes, and neutrophils) were founded in the toxin groups compared with the RM-PL treatment groups (Supporting Information Fig. S8). This infiltration performance of inflammatory leucocytes complied well with the H&E staining results. It was estimated each RM-PL could neutralize 3430 Hlα molecules subcutaneously, nearly 50-fold more than the nanosponge (70 Hlα molecules)[21]. Collectively, these results indicated that RM-PL could successfully prevent skin damage caused by subcutaneous toxin injection. Bacterial infections are commonly localized to the skin and soft tissues and display broad antibiotic resistance, and these distinctive features make the detoxification of PFTs by RM-PL composed of RBC membranes and lipid membranes an attractive treatment.

3.4. *In vivo detoxification of PFTs by RM-PL following intravenous challenge*

The systemic toxin-neutralizing capability of RM-PL was demonstrated through the intravenous injection route. A lethal dose of each toxin (Hlα: 250 μg/kg, LLO: 440 μg/kg, SLO: 500 μg/kg) was injected into ICR mice to generate a toxin-challenged mouse model. RM-PL were injected 2 min after toxin challenge, and PBS was injected in parallel as controls. The results revealed that all mice treated with PBS died within 4 h (Fig. 5A–C). In contrast, all mice treated with RM-PL resisted PFT toxicity and survived until the end of the experiment. H&E staining demonstrated that PFTs caused observable damage to certain organs of mice. Hlα and LLO caused severe hemorrhage in the lung and the kidney (Fig. 5D, E, Supporting Information Figs. S9 and S10). It has been previously reported that alveolar epithelial cells represent sensitive targets to an Hlα assault[36,37], since the pore-forming toxin increases the permeability of the lung to fluid and impairs the alveolar-capillary barrier of the lung in a rat model of *S. aureus*-induced pneumonia[38]. Moreover, pulmonary toxicity of LLO can be due to the dysfunction in the epithelial sodium channel (ENaC) channel in lung microvascular endothelial cells, which weakens the capillary barrier function[36]. SLO induced impaired cardiac muscle as previously reported[39,40] and liver damage (Fig. 5F and Supporting Information Fig. S11). In contrast, histological analysis showed similar appearance between the RM-PL treatment group and the PBS (normal) group with no noticeable irregularities (Fig. 5D–F).

Therefore, since RM-PL neutralized PFT toxicity *in vivo* and avoided toxic effect of PFTs to organs, the toxin-challenged mice saved their lives. PFTs exist widely in nature and are found not only in bacterial exotoxins but also in venom produced by animals such as snakes, bees, scorpions, and anemones[41–43]. Although different PFTs display diverse molecular structures and distinct targets, all disrupt cells by forming pores in the plasma membrane and altering the permeability of the target cell membrane. Since RBCs are the major target cells of various PFTs, RM-PL provide a promising nanoantidote with broad applicability, and their use can potentially be explored to treat most of PFT-related diseases. Regarding to the clinical translation of these biomimetic hybrid nanovesicles, we first need to determine the feasibility of RM-PL made from human RBCs (hRM-PL) to treat established toxin infection. Similar to mouse RBCs, human RBCs contain numerous surface antigens that can be classified to many different blood types. Thus, immuno-compatibility should be ensured through matching hRM-PL with patients according to their blood types (A, B, AB, or O type) and Rh factor (Rh positive or Rh negative) with a crossmatch test, similar to the process used in a blood transfusion. A previous study which utilized nanosponges made from human RBCs to neutralize various PFTs provided a reference for future translational research of hRM-PL[23]. In terms of the dosage form of hRM-PL to treat toxin infections, this biomimetic nanoagent can be formulated into hydrogels for topical applications in the treatment of skin toxin infections[44]. It also could be prepared as an injection or a pulmonary inhalation drug delivery system for the management of systemic toxin infections[21].

3.5. *Biodistribution of RM-PL+Hlα after intravenous injection*

Since RM-PL exhibited excellent detoxification capacity both subcutaneously and intravenously, the mechanism of how the toxin absorbed onto RM-PL was cleared *in vivo* was unknown. Therefore, to investigate the systemic behavior of RM-PL absorbing toxin, DiD-labeled RM-PL was incubated with a model toxin Hlα (RM-PL+Hlα) and injected into mice. To investigate whether Hlα was absorbed by RM-PL after injection, DiD-labeled RM-PL was injected 2 min after Hlα injection [RM-PL(Hlα)]. As shown in Fig. 6A, although both RM-PL+Hlα and RM-PL(Hlα) still exhibited long circulation profiles, the MRT and $t_{1/2}$ for both RM-PL+Hlα and RM-PL(Hlα) were significantly lower than those for free RM-PL (Supporting Information Table S1). RM-PL+Hlα and RM-PL(Hlα) demonstrated similar circulation profiles and there were no differences in the pharmacokinetics parameters (*e.g.*, MRT, AUC, $t_{1/2}$ and Cl) between the two groups. These results indicated that RM-PL could capture toxin *in vivo* and toxin neutralization accelerated the clearance of RM-PL in the blood. We next investigated the *in vivo* tissue distribution of the RM-PL+Hlα. As shown in Fig. 6B, the two primary organs of the mononuclear phagocyte system (MPS), the liver and the spleen, contained more RM-PL than other organs. Intriguingly, there were no significant differences in RM-PL in the liver or in the spleen between the RM-PL+Hlα and RM-PL(Hlα) groups. Compared with the RM-PL group, RM-PL accumulated significantly more in the spleen or in the liver in the RM-PL+Hlα and RM-PL(Hlα) groups. These

results suggest RM-PL could capture toxin *in vivo* and tended to distribute in MPS-related organs.

After providing an organ-level view of RM-PL+Hlα clearance, we then proceeded to analyze sub-organ biodistribution of RM-PL+Hlα in the spleen and in the liver (Fig. 6C-F). Splenocytes were isolated from mice treated with DiD-labeled RM-PL+Hlα and intracellular uptake of RM-PL+Hlα in various immune cells was analyzed by flow cytometry (Fig. 6C and Supporting Information Fig. S12). RM-PL+Hlα was mainly taken up by F4/80$^+$ macrophages in the spleen, while CD11c$^+$ dendritic cells (DC), an important class of antigen-presenting cells, and undifferentiated monocytes also took up part of RM-PL+Hlα (Fig. 6E and Supporting Information Fig. S13). In addition, the cellular phenotype in the liver responsible for RM-PL+Hlα uptake was examined (Fig. 6D and Supporting Information Fig. S14). It was shown that Kupffer cells (F4/80$^+$) in the liver took up most of RM-PL+Hlα, and the endothelial cells (CD31$^+$) took up part of RM-PL+Hlα, while T cells (CD3$^+$), B cells (CD19$^+$) and other cells hardly internalized RM-PL+Hlα (Fig. 6F). Considering the relative amount of each cell subtype in the liver, it was founded that endothelial cells and kupffer cells took up almost equal amount of RM-PL+Hlα (Supporting Information Fig. S15). These results collectively suggest that phagocytic cells dominated by macrophages in the spleen and the liver took up RM-PL+Hlα more efficiently than other cells, playing an important role in detoxification.

3.6. *Cellular uptake of RM-PL+Hlα*

Based on the above results, we further verified that macrophages in the spleen and the liver took up the detoxified nanoparticles by immunofluorescence staining. At 18 h after injection, the co-localization of macrophages and RM-PL+Hlα can be clearly seen in the liver (Fig. 7A, B) and spleen sections (Fig. 7C, D), indicating RM-PL+Hlα was processed and taken up by the macrophages. These data correlated well to the results determined by flow cytometry (Fig. 6E and F).

We next examined the cellular uptake behavior of RM-PL+Hlα on macrophages (RAW 264.7) *in vitro*. The cellular uptake of RM-PL+Hlα was time-dependent (Fig. 7E and Supporting Information Fig. S16A). At 4 h after incubation, the cell uptake rate reached nearly 100% (Fig. S16A), so it was determined as the incubation time for subsequent uptake experiments. In addition, it could be seen that the cells exhibited obvious uptake of the RM-PL+Hlα after incubating for 4 h (Fig. S16B).

Macrophages could internalize nanoparticles avidly through a variety of mechanisms, including constitutive macropinocytosis, receptor-mediated endocytosis and phagocytosis. To clarify the endocytosis pathway involved in RM-PL+Hlα internalization by macrophages, cellular uptake analysis was conducted in the presence of different inhibitors. Genistein and chlorpromazine were employed to block caveolin-mediated and clathrin-mediated endocytosis, respectively. Cytochalasin D was an inhibitor of phagocytosis and macropinocytosis by blocking actin polymerization. Amiloride and mβCD could inhibit macropinocytosis through different mechanisms of action. 4 °C was selected to investigate the impact of energy on the cellular uptake. As shown in Fig. 7F, G, almost all of the indicators inhibited the cellular internalization of RM-PL+Hlα, especially pre-incubation at 4 °C. Specifically, the cellular uptake of RM-PL+Hlα was inhibited by 73.3%, 46%, 63.9%, 56.9% and 65.5% in the presence of amiloride, genistein, mβCD, cytochalasin D and chlorpromazine, respectively, suggesting various endocytic processes were involved in RM-PL+Hlα by macrophages. Furthermore, because endocytosis was an energy-consuming process, the low-temperature treatment could strongly inhibit endocytosis of RM-PL+Hlα.

The subcellular localizations of RM-PL absorbing toxin in macrophages have a critical impact on their detoxification mechanism. In an effort to explore precise subcellular localization of RM-PL+Hlα after internalization, confocal fluorescence imaging of macrophages internalizing RM-PL+Hlα was performed. To identify the intracellular compartment where RM-PL+Hlα was enriched, LysoGreen, a lysosome marker which selectively accumulates in cellular compartments with low internal pH, was used to investigate the co-localization of DiD-labeled RM-PL+Hlα with lysosomes in RAW264.7 cells. As shown in Fig. 7H and Supporting Information Fig. S17, the cellular uptake of RM-PL+Hlα and the co-localization RM-PL+Hlα with lysosomes increased with time and reached the platform at 6 h after incubation. At 6 and 24 h after incubation, almost all RM-PL+Hlα was localized in lysosomes, suggesting that nearly all RM-PL+Hlα was finally transported to lysosomes for digestion. Specifically, there was a shift of DiD signal from punctate (6 h) to diffusive pattern (24 h) as revealed by confocal laser scanning microscopy. Since DiD was a lipophilic fluorescent dye for labeling membranes and other hydrophobic structures, it might diffuse into the membrane components inside the cell after the digestion of RM-PL+Hlα by lysosome enzymes, and therefore a diffusive pattern of DiD fluorescence was observed with time. This time-dependent finding was taken as an indication that RM-PL+Hlα was digested and detoxified in lysosomes after endocytosis by macrophages. Meanwhile, chloroquine, a known lysosomotropic agent that interferes with lysosomal acidification, was utilized to further confirm the role of lysosomes in toxin detoxification. As shown in Supporting Information Fig. S18, the internalization of RM-PL+Hlα was reduced by nearly 50% in chloroquine-treated RAW264.7 cells when compared to non-treated macrophages. These findings together suggest that RM-PL+Hlα was digested and detoxified in lysosomes after endocytosis by macrophages.

To investigate the role of RM-PL and RM-PL+Hlα on macrophage polarization, a flow cytometry assay was employed. The results showed that both RM-PL and RM-PL+Hlα could promote macrophage polarization into M1-like phenotype as indicated by the upregulation of the M1 marker levels of CD80 and CD86 and the down-expression of CD206 (Supporting Information Fig. S19). Interestingly, there was no statistically significant differences in macrophage polarization between RM-PL and RM-PL+Hlα groups, suggesting that RM-PL+Hlα was safely processed by macrophages without triggering additional immune responses.

4. Conclusions

In this study, erythroliposome (RM-PL) was successfully formulated for neutralizing a series of hemolytic PFTs. Consisting of safe artificial lipids and natural RBC membranes, the resulting RM-PL bore a stable bilayer structure. When mixed with three different types of toxins (α-hemolysin, listeriolysin O, and streptolysin O), RM-PL was highly effective in completely inhibiting the toxins' hemolytic activity both *in vitro* and *in vivo*. More impressively, the neutralized toxin lost its original toxicity to target organs, allowing animals to survive healthily. In contrast,

the free toxins caused serious damage to animal organs and eventually lead to the death of animals within a few hours when applied in a similar manner as the sequestered counterparts. It was found that the toxins absorbed by RM-PL were taken to the liver and spleen, and then endocytosed and digested by macrophages in the two organs through a variety of endocytosis pathways. Overall, this work provided not only a promising platform for broad-spectrum PFT neutralization but also a deeper understanding of the detoxification mechanism.

Acknowledgments

This project was supported by the National Natural Science Foundation of China (81773283). Thanks were given to the staff members of the Electron Microscopy System and Integrated Laser Microscopy System at the National Facility for Protein Science in Shanghai (NFPS), Zhangjiang Lab (China) for providing technical support and assistance in data collection and analysis.

Author contributions

Zhiqing Pang designed the project. Chunying Liu carried out the experiments and performed data analysis. Shuangrong Ruan, Ying He, Xuejing Li and Yuefei Zhu participated in part of the experiments. Honglan Wang and Hanwei Huang provided experimental drugs and quality control. Chunying Liu wrote the manuscript. Zhiqing Pang revised the manuscript. All of the authors have read and approved the final manuscript.

Conflicts of interest

The authors declare no conflicts of interest.

Appendix A. Supplementary data

Supplementary data to this article can be found online at https://doi.org/10.1016/j.apsb.2022.03.015.

References

1. Theuretzbacher U, Outterson K, Engel A, Karlen A. The global preclinical antibacterial pipeline. *Nat Rev Microbiol* 2020;**18**:275−85.
2. Czaplewski L, Bax R, Clokie M, Dawson M, Fairhead H, Fischetti VA, et al. Alternatives to antibiotics—a pipeline portfolio review. *Lancet Infect Dis* 2016;**16**:239−51.
3. Theuretzbacher U, Gottwalt S, Beyer P, Butler M, Czaplewski L, Lienhardt C, et al. Analysis of the clinical antibacterial and antituberculosis pipeline. *Lancet Infect Dis* 2019;**19**:E40−50.
4. Willyard C. The drug-resistant bacteria that pose the greatest health threats. *Nature* 2017;**543**:15.
5. Beyer P, Paulin S. The antibacterial research and development pipeline needs urgent solutions. *ACS Infect Dis* 2020;**6**:1289−91.
6. Chaudhary AS. A review of global initiatives to fight antibiotic resistance and recent antibiotics' discovery. *Acta Pharm Sin B* 2016;**6**:552−6.
7. Baker SJ, Payne DJ, Rappuoli R, De Gregorio E. Technologies to address antimicrobial resistance. *Proc Natl Acad Sci U S A* 2018;**115**:12887−95.
8. Verma P, Gandhi S, Lata K, Chattopadhyay K. Pore-forming toxins in infection and immunity. *Biochem Soc Trans* 2021;**49**:455−65.
9. Li SH, Leung PHM, Xu XY, Wu CH. Homogentisic acid gamma-lactone suppresses the virulence factors of pseudomonas aeruginosa by quenching its quorum sensing signal molecules. *Chin Chem Lett* 2018;**29**:313−6.
10. Dal Peraro M, van der Goot FG. Pore-forming toxins: ancient, but never really out of fashion. *Nat Rev Microbiol* 2016;**14**:77−92.
11. Los FC, Randis TM, Aroian RV, Ratner AJ. Role of pore-forming toxins in bacterial infectious diseases. *Microbiol Mol Biol Rev* 2013;**77**:173−207.
12. Bezrukov SM, Nestorovich EM. Inhibiting bacterial toxins by channel blockage. *Pathog Dis* 2016;**74**.
13. Escajadillo T, Nizet V. Pharmacological targeting of pore-forming toxins as adjunctive therapy for invasive bacterial infection. *Toxins* 2018;**10**:542.
14. Nestorovich EM, Bezrukov SM. Obstructing toxin pathways by targeted pore blockage. *Chem Rev* 2012;**112**:6388−430.
15. Muhlen S, Dersch P. Anti-virulence strategies to target bacterial infections. *Curr Top Microbiol Immunol* 2016;**398**:147−83.
16. Rasko DA, Sperandio V. Anti-virulence strategies to combat bacteria-mediated disease. *Nat Rev Drug Discov* 2010;**9**:117−28.
17. Gao W, Chen Y, Zhang Y, Zhang Q, Zhang L. Nanoparticle-based local antimicrobial drug delivery. *Adv Drug Deliv Rev* 2018;**127**:46−57.
18. Rainey GJ, Young JA. Antitoxins: novel strategies to target agents of bioterrorism. *Nat Rev Microbiol* 2004;**2**:721−6.
19. Page R, Peti W. Toxin-antitoxin systems in bacterial growth arrest and persistence. *Nat Chem Biol* 2016;**12**:208−14.
20. Fang RH, Luk BT, Hu CM, Zhang L. Engineered nanoparticles mimicking cell membranes for toxin neutralization. *Adv Drug Deliv Rev* 2015;**90**:69−80.
21. Hu CM, Fang RH, Copp J, Luk BT, Zhang L. A biomimetic nanosponge that absorbs pore-forming toxins. *Nat Nanotechnol* 2013;**8**:336−40.
22. Hu CM, Zhang L, Aryal S, Cheung C, Fang RH, Zhang L. Erythrocyte membrane-camouflaged polymeric nanoparticles as a biomimetic delivery platform. *Proc Natl Acad Sci U S A* 2011;**108**:10980−5.
23. Chen Y, Chen M, Zhang Y, Lee JH, Escajadillo T, Gong H, et al. Broad-spectrum neutralization of pore-forming toxins with human erythrocyte membrane-coated nanosponges. *Adv Healthc Mater* 2018;**7**:e1701366.
24. Henry BD, Neill DR, Becker KA, Gore S, Bricio-Moreno L, Ziobro R, et al. Engineered liposomes sequester bacterial exotoxins and protect from severe invasive infections in mice. *Nat Biotechnol* 2015;**33**:81−8.
25. He Y, Li R, Li H, Zhang S, Dai W, Wu Q, et al. Erythroliposomes: Integrated hybrid nanovesicles composed of erythrocyte membranes and artificial lipid membranes for pore-forming toxin clearance. *ACS Nano* 2019;**13**:4148−59.
26. Salam KA, Wang RY, Grandinetti T, De Giorgi V, Alter HJ, Allison RD. Binding of free and immune complex-associated hepatitis c virus to erythrocytes is mediated by the complement system. *Hepatology* 2018;**68**:2118−29.
27. Sharma R, Zhao H, Al-Saleem FH, Ubaid AS, Puligedda RD, Segan AT, et al. Mechanisms of enhanced neutralization of botulinum neurotoxin by monoclonal antibodies conjugated to antibodies specific for the erythrocyte complement receptor. *Mol Immunol* 2014;**57**:247−54.
28. Dehaini D, Wei XL, Fang RH, Masson S, Angsantikul P, Luk BT, et al. Erythrocyte-platelet hybrid membrane coating for enhanced nanoparticle functionalization. *Adv Mater* 2017;**29**:8.
29. Magarkar A, Dhawan V, Kallinteri P, Viitala T, Elmowafy M, Rog T, et al. Cholesterol level affects surface charge of lipid membranes in saline solution. *Sci Rep* 2014;**4**:5005.
30. Kaddah S, Khreich N, Kaddah F, Charcosset C, Greige-Gerges H. Cholesterol modulates the liposome membrane fluidity and permeability for a hydrophilic molecule. *Food Chem Toxicol* 2018;**113**:40−8.
31. Tweten RK. Cholesterol-dependent cytolysins, a family of versatile pore-forming toxins. *Infect Immun* 2005;**73**:6199−209.

32. Jaspard F, Nadi M, Rouane A. Dielectric properties of blood: an investigation of haematocrit dependence. *Physiol Meas* 2003;**24**:137−47.
33. Hochmuth RM, Evans CA, Wiles HC, McCown JT. Mechanical measurement of red cell membrane thickness. *Science* 1983;**220**:101−2.
34. Rawicz W, Olbrich KC, McIntosh T, Needham D, Evans E. Effect of chain length and unsaturation on elasticity of lipid bilayers. *Biophys J* 2000;**79**:328−39.
35. Hu CM, Fang RH, Copp J, Luk BT, Zhang L. A biomimetic nanosponge that absorbs pore-forming toxins. *Nat Nanotechnol* 2013;**8**:336−40.
36. Lucas R, Hadizamani Y, Gonzales J, Gorshkov B, Bodmer T, Berthiaume Y, et al. Impact of bacterial toxins in the lungs. *Toxins* 2020;**12**:223.
37. Rose F, Dahlem G, Guthmann B, Grimminger F, Maus U, Hänze J, et al. Mediator generation and signaling events in alveolar epithelial cells attacked by *S. Aureus* alpha-toxin. *Am J Physiol Lung Cell Mol Physiol* 2002;**282**:L207−14.
38. Hermann I, Räth S, Ziesemer S, Volksdorf T, Dress RJ, Gutjahr M, et al. Staphylococcus aureus hemolysin a disrupts cell-matrix adhesions in human airway epithelial cells. *Am J Respir Cell Mol Biol* 2015;**52**:14−24.
39. Halpern BN, Rahman S. Studies on the cardiotoxicity of streptolysin O. *Br J Pharmac Chemother* 1968;**32**:441−52.
40. Bolz DD, Li Z, McIndoo ER, Tweten RK, Bryant AE, Stevens DL. Cardiac myocyte dysfunction induced by streptolysin O is membrane pore and calcium dependent. *Shock* 2015;**43**:178−84.
41. Andreeva-Kovalevskaya Zh I, Solonin AS, Sineva EV, Ternovsky VI. Pore-forming proteins and adaptation of living organisms to environmental conditions. *Biochemistry* 2008;**73**:1473−92.
42. Xie CF, Slagboom J, Albulescu LO, Somsen GW, Vonk FJ, Casewell NR, et al. Neutralising effects of small molecule toxin inhibitors on nanofractionated coagulopathic crotalinae snake venoms. *Acta Pharm Sin B* 2020;**10**:1835−45.
43. Dang BB. Chemical synthesis and structure determination of venom toxins. *Chin Chem Lett* 2019;**30**:1369−73.
44. Wang F, Gao W, Thamphiwatana S, Luk BT, Angsantikul P, Zhang Q, et al. Hydrogel retaining toxin-absorbing nanosponges for local treatment of methicillin-resistant staphylococcus aureus infection. *Adv Mater* 2015;**27**:3437−43.